Characterization of aerosol hygroscopicity using Raman lidar measurements at the EARLINET station of Payerne

Francisco Navas-Guzmán[1], Giovanni Martucci[1], Martine Collaud Coen[1], María José Granados-Muñoz[2], Maxime Hervo[1], Michael Sicard[2,3], and Alexander Haefele[1,4]

[1]Federal Office of Meteorology and Climatology MeteoSwiss, Payerne, Switzerland
[2]Remote Sensing Laboratory/CommSensLab, Universitat Politècnica de Catalunya, 08034 Barcelona, Spain
[3]Ciències i Tecnologies de l'Espai - Centre de Recerca de l'Aeronàutica i de l'Espai / Institut d'Estudis Espacials de Catalunya (CTE-CRAE / IEEC), Universitat Politècnica de Catalunya, Barcelona, 08034, Spain
[4]Department of Physics and Astronomy, The University of Western Ontario, London, Canada

Correspondence: Francisco Navas Guzmán (francisco.navas@meteoswiss.ch)

Abstract. This study focuses on the analysis of aerosol hygroscopicity using remote sensing technique. Continuous observations of aerosol backscatter coefficient (β^{aer}), temperature (T) and water vapour mixing ratio (r) are performed by means of a Raman lidar system at the aerological station of MeteoSwiss at Payerne (Switzerland) since 2008. These measurements allow us to monitor in a continuous way any change of aerosol properties as a function of the relative humidity (*RH*). These changes can be observed either in time at constant altitude or in altitude at a constant time. The accuracy and precision of *RH* measurements from the lidar have been evaluated using the radiosonde (RS) technique as reference. A total of 172 RS profiles were used in this intercomparison which revealed a bias smaller than 4%RH and a standard deviation smaller than 10%RH between both techniques in the whole (in lower) troposphere at nightime (at daytime), indicating the good performance of the lidar for characterizing *RH*. A methodology to identify situations favorable to study aerosol hygroscopicity has been established and the aerosol hygroscopicity has been characterized by means of the backscatter enhancement factor (f_β). Two case studies, corresponding to different types of aerosol are used to illustrate the potential of this methodology. The first case corresponds to a mixture of rural aerosol and smoke particles (smoke mixture), which showed a higher hygroscopicity (f_β^{355} = 2.8 and f_β^{1064} = 1.8 in the *RH* range 73% - 97%) than the second case, in which mineral dust was present (f_β^{355} = 1.2 and f_β^{1064} = 1.1 in the *RH* range 68% - 84%). The higher sensitivity of the shortest wavelength to hygroscopic growth was qualitatively reproduced using Mie simulations. In addition, a good agreement was found between the hygroscopic analysis done in the vertical and in time for case I, where the latter also allowed to observe the hydration and dehydration of the smoke mixture. Finally, the impact of aerosol hygroscopicity on the Earth's radiative balance has been evaluated using the GAME (Global Atmospheric Model) radiative transfer model. The model showed an impact with an increase in absolute value of 2.4 W/m^2 at the surface with respect to the dry conditions for the hygroscopic layer of Case I (smoke mixture).

1 Introduction

Atmospheric aerosol particles scatter and absorb solar radiation and therefore have an impact on the Earth's radiative budget (direct effect). In addition, aerosol particles can act as cloud condensation nuclei (CCN) and modify cloud microphysical properties also altering the global radiative budget (indirect effects) in this way (Haywood and Boucher, 2000). The uncertainty in assessing total anthropogenic greenhouse gas and aerosol impacts on climate must be substantially reduced from its current level to allow meaningful predictions of future climate. This uncertainty is currently dominated by the aerosol component (Bindoff et al., 2013). Evaluation of aerosol effects on climate must take into account high spatial and temporal variation of aerosol concentrations and properties as well as the aerosol interactions with clouds and its influence on precipitation. During the last years a huge effort was made to characterize vertically-resolved profiles of optical and microphysical properties for different kinds of particles. Raman lidars (light detection and ranging) have proven to be an essential tool to obtain profiles of these properties without modifying the environmental conditions (Ansmann et al., 1992; Navas-Guzmán et al., 2013; Granados-Muñoz et al., 2014). Networks like EARLINET (European Aerosol Research Lidar Network) have contributed to create a quantitative, comprehensive, and statistically significant database for the horizontal, vertical, and temporal distribution of aerosols on a continental scale (Bösenberg et al., 2003; Pappalardo et al., 2014; Sicard et al., 2015).

However, despite of the big effort of the scientific community to characterize aerosol effects, there are some processes that are not well understood yet. For example, an important factor that can modify the role of aerosols in the global energy budget is *RH*. Under high *RH* conditions, aerosol particles may uptake water, changing their size and chemical composition (hygroscopic growth). This hygroscopic growth affects the direct scattering of radiation and especially the indirect effects, as the ability of aerosol to act as CCN is directly related to their affinity for water vapour (Hänel, 1976; Feingold and Morley, 2003; Zieger et al., 2013). Thus, understanding aerosol hygroscopic growth is of high importance to quantify the influence of atmospheric aerosol in climate models or for comparisons of remote sensing with in-situ measurements which are often performed under dry conditions (Zieger et al., 2010).

Several studies have addressed the characterization of aerosol hygroscopicity using in-situ measurements over the last years. Techniques as the Humidified Tandem Differential Mobility Analyzer (HT-DMA) (e.g.Swietlicki et al. (2008)) or Humidified tandem nephelometers have been extensively used to quantify the change in particle diameter or aerosol optical properties due to water uptake (Pilat and Charlson, 1966; Fierz-Schmidhauser et al., 2010; Zieger et al., 2013). However, despite of the great contribution that these techniques can provide to the understanding of the aerosol hygroscopic processes they also present some shortcomings. For example, most in situ techniques are limited by the fact that they modify the ambient conditions and are also subject to particle losses in the sampling lines, thereby altering the real atmospheric aerosol properties (Bedoya-Velásquez et al., 2018). In addition, they present larger errors in the characterization of the aerosol hygroscopicity for high *RH* (conditions close to saturation), specially when the aerosol is more hygroscopic (Titos et al., 2016).

In this sense, remote sensing techniques could overcome theses difficulties since they can provide vertically resolved measurements without modifying the aerosol sample. In addition, they are also able to measure under *RH* close to saturation, that is where particles are more affected by hygroscopic growth (Feingold and Morley, 2003). However, the number of aerosol hygro-

scopic studies using remote sensing is modest and most of them were limited to specific field campaigns. The main limitation to address these studies comes from the difficulty to obtain *RH* profiles with high vertical and temporal resolution. Most of the studies carried out so far have used sensors to measure *RH* on board of RS or aircrafts or in meteorological towers in combination with the aerosol measurements from lidars to investigate the aerosol hygroscopicty (Wulfmeyer and Feingold, 2000; Veselovskii et al., 2009; Granados-Muñoz et al., 2015; Haeffelin et al., 2016; Lv et al., 2017; Zhao et al., 2017; Fernández et al., 2018). Recently, the combination of *T* profiles from microwave radiometers (MWR) and *r* profiles from Raman lidar have been used to retrieve *RH* profiles (Navas-Guzmán et al., 2014) and applied to aerosol hygroscopic studies (Bedoya-Velásquez et al., 2018). However, although this synergy of instrumentation can be a good solution for many stations the uncertainties coming from MWR *T* profiles can be problematic due to its lower spatial resolution (Navas-Guzmán et al., 2016). In addition, most of the *r* measurements from Raman lidar system are limited to night-time observations, due to the low signal-to-noise ratio (SNR) of the Raman channels during daytime.

In the present study we show the capability of the RAman Lidar for Meteorological Observations (RALMO) operated at the aerological station of MeteoSwiss at Payerne (Switzerland) to monitor aerosol hygroscopicity based on its continuous aerosol and *RH* measurements. The methodology needed for this characterization is introduced and applied to two case studies in which different aerosol types were present.

2 Experimental site and instrumentation

Data from collocated remote sensing and in-situ sensors were acquired at the aerological station of MeteoSwiss at Payerne (Switzerland, 46.82° N, 6.95° E, 491 m above sea level (asl)). The station is located in a rural area on the Swiss Plateau, between the Jura mountains (25 km to north-west) and the Alpine foothills (20 km to the south-east). The site is not significantly affected by industrial pollution and the region is characterized by a mid-latitude continental climate.

Aerosol vertical information is mainly obtained from lidar systems installed at the station. RALMO is the main tool of this study and was developed by the Swiss Federal Institute of Technology (EPFL) in collaboration with MeteoSwiss and is operated at MeteoSwiss Payerne since August 2008. The instrument is dedicated to operational meteorology, model validation, climatological studies as well as ground truthing of satellite data. The lidar was specially designed to satisfy the requirements for operational monitoring of the atmosphere and to create a durable and homogeneous dataset to be used for climatology studies (Dinoev et al., 2013). The lidar system uses a Nd:YAG laser source which emits pulses of 8 ns duration at a wavelength of 355 nm and with a repetition rate of 30 Hz. The mean energy per pulse at 355 nm is around 400 mJ. Before being emitted into the atmosphere the beam is expanded to a diameter of 14 cm which reduces the beam divergence (to 0.1 mrad) and ensures eye-safety. The receiving system consists of four telescopes with 30-centimeter parabolic mirrors which are arranged symmetrically around the vertically mounted beam expander to receive the backscattered photons. The total aperture of this telescope system is equivalent to a telescope with a single mirror of 60 cm diameter and it has a field of view of 0.2 mrad. This narrow field of view combined with the narrow-band receiver and high pulse energy allows daytime operation. Optical fibers connect the telescope mirrors with two grating polychromators which allow to isolate the rotational-vibrational Raman signals

of nitrogen and water vapor (wavelengths of 386.7 and 407.5 nm, respectively) as well as the elastic signal and four portions of the pure rotational Raman spectrum around 355 nm for *T*, aerosol backscatter and extinction measurements. The optical signals are finally detected by photomultipliers and acquired by a transient recorder (Brocard et al., 2013). A detailed description of the different parts of this lidar system can be found in Dinoev et al. (2013). RALMO was incorporated into EARLINET in 2008.

In order to gain more spectral information in the profiles of aerosol properties, data from a co-located ceilometer has been used in this study. The ceilometer CHM15k from Lufft company operated at Payerne is a lidar cloud height sensor based on a single wavelength backscattering technique. Its Nd:YAG narrow-beam microchip laser operates at 1064 nm. Cloud layers can be detected in a range of up to 15 km. In addition to the cloud base information, we derive β^{aer} at 1064 nm from the elastic signal using the Klett inversion technique (Klett, 1981).

RS measurements were also used in this study to assess the *T*, *r* and *RH* profiles retrieved from RALMO. The SRS-C50 sondes were flown operationally at Payerne and launched twice a day at 11 UTC and 23 UTC. The sondes were launched and transported through the troposphere and stratosphere by a balloon inflated with Hydrogen and reaching on average 35 km. The vertical resolution of the measured profiles of *T* and humidity is of about 6 m. The sensors of these RSs include copper–constantan thermocouples for *T*, a full range water hypsometer for pressure and a sensor with hygristor for *RH*. The accuracy of these three parameters in the troposphere is 0.1 K for *T*, 2 hPa (accuracy decreases with height) for pressure and 5 to 10% for *RH*.

Sun-photometer measurements have also been included in this study to complement the aerosol information. MeteoSwiss operates four Precision Filter Radiometers (PFR) that were installed in the framework of the international GAW-PFR (Global Atmosphere Watch - Precision Filter Radiometer) program of the World Meteorological Organization (WMO). They measure the direct solar irradiance at the four wavelengths (368, 412, 500 and 862 nm) used in the GAW PFR network as well as 9 additional wavelengths (305, 311, 318, 332, 450, 610, 675, 718, 778, 817, 946 and 1024 nm). Integrated water vapor (IWV) is obtained from the measurements at 718, 817 and 946 nm. The Aerosol Optical Depths (AODs) have been calculated based on the solar irradiance at the different wavelengths using the GAW-PFR algorithms (McArthur et al., 2003). In addition, the AOD Angström exponent (AE) is used in this study as a qualitative indicator of the relative dominance of fine and coarse mode aerosols. Values of AE larger than 1.5 are indicative of a higher fine mode fraction (Nyeki et al., 2012).

In-situ observations at ground-level were also used to complement the column aerosol information obtained from remote sensing. These in-situ measurements at Payerne are carried out by EMPA in the framework of the Nabel (National Air Pollution Monitoring Network) monitoring program. Aerosol absorption coefficients at 7 wavelenghts (from 370 to 950 nm) were obtained from aethalometer measurements (AE31 model). Light absorption measurements at ultraviolet, visible and infrared wavelengths can be used to quantitatively assess the aerosol source contribution (Collaud Coen et al., 2004; Sandradewi et al., 2008; Segura et al., 2014). In addition, concentrations of PM10 and PM2.5 (ambient air levels of atmospheric particulate matter finer than 10 and 2.5 microns) were obtained from an aerosol spectrometer (Fidas 200). These measurements were used to characterize the size of the particles that arrived to our station.

3 Methodology

3.1 Retrievals of *RH* and aerosol property profiles

As mentioned in the introduction, the main practical limitation to study the effect of hygroscopicity on optical and microphysical aerosol properties is the lack of simultaneously and continuously available aerosol and *RH* measurements with a good vertical and temporal resolution. RALMO can overcome this limitation thanks to its capability to perform continuous measurements of *T*, water vapour and aerosol profiles during day and night. In this section the methodology to retrieve these atmospheric parameters from the lidar signals is described.

T measurements are made using the pure-rotational Raman (PRR) technique (Vaughan et al., 1993). An atmospheric *T* profile can be derived from the analysis of the intensities of lines with low and high quantum numbers that have opposite *T* derivatives. A detailed description of the *T* inversion technique applied to our system can be found in Martucci et al. (in preparation).

r is defined as the ratio of the mass of water vapour to the mass of dry air in a sample of the atmosphere (Goldsmith et al., 1998). Profiles of *r* can be obtained from Raman lidar measurements as the ratio of rotational-vibrational Raman scattering intensities from water vapour and nitrogen molecules (Whiteman, 2003a, b; Brocard et al., 2013; Navas-Guzmán et al., 2014). It can be expressed as follows:

$$r(z) = C\frac{S_{H_2O}}{S_{N_2}} \exp\left\{\int_0^z \left[\alpha\left(r,\lambda_{H_2O}\right) - \alpha\left(r,\lambda_{N_2}\right)\right] dr\right\} \tag{1}$$

where *C* is the lidar calibration coefficient that takes into account the fractional volume of nitrogen in the atmosphere (0.78), the instrumental transmission and detection efficiencies at the wavelengths of the Raman returns and the range-independent Raman backscatter cross section for nitrogen and water vapour. The calibration coefficient must be determined for each specific lidar. In the case of RALMO, C is obtained combining absolute calibration with co-located radiosounding, with relative calibration using the solar background (Martucci et al., 2018). S_{H_2O} and S_{N_2} are the Raman lidar signals for water vapour and nitrogen, respectively, after being corrected for saturation and background. The exponential term is the difference in the atmospheric transmission between the surface and the altitude z for nitrogen (386.7 nm) and water vapour (407.5 nm). The molecular extinction is calculated considering US Standard Atmosphere. For normal conditions at Payerne the effect of differential extinction due to aerosols between these two wavelengths is small and is neglected (Dinoev et al., 2013). However, when this differential extinction is not negligible, Muñoz-Porcar et al. (2018) showed that it can accurately be calculated using a radiative transfer model with a relatively simple parametrization.

RH profiles are obtained combining *T* and *r*. *RH* is defined as the ratio of the actual amount of water vapour in the air compared to the equilibrium amount (saturation) at that *T* (Yau and Rogers, 1996), and it can be calculated as:

$$RH(z) = \frac{e(z)}{e_w(z)} \times 100, \tag{2}$$

where $e(z)$ is the water vapour pressure while $e_w(z)$ is referred to the saturation pressure. The water vapour pressure is related to *r* as follows:

$$e(z) = \frac{p(z)r(z)}{0.622 + r(z)}, \tag{3}$$

where $p(z)$ is the air pressure profile which can be estimated from RS or assuming a US standard atmosphere. In our case, and thanks to the availability of operational RS measurements in our station, the closest RS in time is used to calculate the pressure profile. For saturation pressure we use the following expression:

$$e_w(z) = 6.107 \exp\left[\frac{M_A\,[T(z) - 273]}{M_B + [T(z) - 273]}\right], \tag{4}$$

where the constants M_A and M_B are 17.84 (17.08) and 245.4 (234.2), respectively, for *T* below (above) 273 K (List, 1951).

Aerosol vertical information is also retrieved from RALMO measurements. The backscattered radiation from aerosols and molecules due to Mie and Rayleigh scattering, respectively, has the same wavelength as the laser and is referred as the elastic signal, $S_{El}(z)$. Stokes and anti-Stokes portions of the PRR spectrum with opposite *T* dependence are summed, giving in good approximation a *T* independent inelastic signal $S_{PRR}(z)$. β^{aer} is derived from the ratio between the elastic and inelastic signals as follows:

$$\beta^{aer}(z) = \beta^{mol}(z)\left[k\frac{S_{El}(z)}{S_{PRR}(z)} - 1\right], \tag{5}$$

where k is the calibration constant and β^{mol} is the molecular backscatter coefficient. β^{mol} is calculated using a measured atmospheric density while the k constant is estimated assuming a molecular behaviour of the atmosphere in the far range (upper troposphere).

3.2 Selection of aerosol hygroscopic cases

Continuous measurements of aerosol and *RH* profiles from RALMO lidar allow to monitor any change in aerosol properties that could occur as result of the water uptake by particles under high *RH* (aerosol hygroscopic growth). However, to ensure that the changes in the aerosol properties are due to hygroscopic growth and not to changes in the load or composition of the aerosol certain requirements must be fulfilled.

As a first condition an increase in β^{aer} should occur simultaneously with an increase in *RH*. This condition could be observed in the vertical for a certain aerosol layer (vertical hygroscopic growth) but it could also be found as a function of time at a constant altitude. It is worth to remark that RALMO is one of the few remote sensing instruments in the world that is able to monitor those processes as a function of time and height. Cases fulfilling the previous condition were selected as potential cases of hygroscopic growth. After that, we needed to ensure a high degree of homogeneity in the investigated aerosol layer. For that, a second requirement to be fulfilled is that the origin of the air masses, in the region where the presence of hygroscopicity is assessed, is independent of altitude (in case of vertical hygroscopic growth). To guarantee that, we have used backward trajectory analysis from HYSPLIT model (Hybrid Single-Particle Lagrangian Integrated Trajectory) (Draxler and Rolph, 2003). As final condition to ensure a good mixing within the layer we used the profiles of *r* and potential temperature (θ)

obtained from RALMO measurements. Slow-varying or constant values of these two parameters are indicative of well-mixed conditions across the aerosol layer.

Similar criteria to assess the homogeneity of an aerosol layer were required in previous studies using remote sensing (Veselovskii et al., 2009; Granados-Muñoz et al., 2015; Bedoya-Velásquez et al., 2018). However, this is the first time that the profiles of *r* and θ are obtained from the same instrument as the aerosol measurements. It presents a clear advantage since all the parameters are measured for the same atmospheric column as opposed to studies using RSs or MWR.

Another novelty of this study is the capability to monitor aerosol hygroscopic growth in time at different altitudes in the troposphere. For this temporal analysis we used the *r* measurements to ensure that changes of aerosol properties in time are only due to hygroscopic processes. In the absence of condensation and evaporation processes *r* can be considered an atmospheric tracer and we assume that an air parcels with the same *r* have in good approximation the same origin and hence the same aerosol load and composition. In addition, wind measurements from a collocated wind profiler are used to corroborate that the wind direction was the same during the analyzed period.

Once all the previous requirements have been fulfilled the aerosol hygroscopicity is characterized by means of the f_β. This parameter is defined as

$$f_\zeta(RH) = \frac{\zeta(RH)}{\zeta(RH_{ref})} \tag{6}$$

where $\zeta(RH)$ represents an aerosol property at a certain *RH*. RH_{ref} is the so-called reference *RH* and it is chosen as the lowest value of *RH* in the analyzed layer or time interval. In this study, f_β has been calculated for β^{aer}.

In order to be able to compare our results with other studies in which RH_{ref} or the *RH* range could be different the humidograms (*RH* versus the f_β) are parameterized using fitting equations (e.g. Titos et al. (2016)). In this study we use the one-parameter equation introduced by Hänel (1976), which has been used in other hygroscopic studies using remote sensing (Granados-Muñoz et al., 2015; Bedoya-Velásquez et al., 2018). The general form of the Hänel equation is expressed as

$$f_\zeta(RH) = \left(\frac{1 - RH/100}{1 - RH_{ref}/100}\right)^{-\gamma} \tag{7}$$

where γ is an indicator of the aerosol hygroscopicity. Larger values of γ indicate higher hygroscopicity.

4 Validation of lidar measurements versus operational RSs

Since data quality is critical, a validation with respect to the RS technique has been carried out, which we consider the reference. As it was indicated in Section 2, operational RS are launched twice per day at the aerological station of Payerne. The availability of simultaneous lidar and RS measurements at our station allowed us to minimize the differences due to spatio-temporal inhomogeneities.

Figure 1 shows the *r*, *T* and *RH* profiles obtained from RALMO lidar and RS at nighttime (23:00 UTC) on 20th September 2017. A very good agreement can be observed from this figure for the three atmospheric parameters. We can see that RALMO provided very accurate results even for altitude ranges where strong gradients were observed, as for the wet layer located above

2 km above ground level (agl) or for the *T* inversion observed at 1.7 km (agl). Mean and standard deviation for the whole profile (from ground to 8 km (agl)) of the relative differences in *r* were $-1 \pm 13\%$, while mean and standard deviation of *T* and *RH* differences were -0.1±0.7 K and -1±6 %RH, respectively. This example shows the potential of RALMO to provide accurate measurements with a good spatial resolution. In order to evaluate the accuracy and the precision of RALMO retrievals, a statistical analysis of lidar and RS differences was carried out. A total of 172 RS were used in this intercomparison during day- and night-time for the period from July to December of 2017. The *T* validation of RALMO lidar is discussed in more depth in a separate paper (Martucci et al., in preparation). Here we would only like to discuss the statistics for this 6-month period. For night-time measurements (23:00 UTC), a total of 100 RS were used to compare with lidar and the mean *T* deviation profile evidenced a small bias of 0.05 ± 0.06 K in the first 5 km and 0.15 ± 0.15 K above that altitude. The standard deviation profile also confirmed the excellent performance of RALMO retrieving *T* with standard deviations below 1 K in the full troposphere (mean values of 0.6 ± 0.1 K below 5 km (agl) and 1.00 ± 0.16 K above). For daytime measurements (11:00 UTC), 72 pairs of profiles were used. The mean *T* deviations between lidar and RS for daytime measurements were of -0.5 ± 0.2 K in the lower troposphere (0-5 km agl) and -0.1 ± 0.6 in the upper troposphere (5-10 km agl). The *T* standard deviations were 0.8 ± 0.2 and 2.4 ± 0.8 for the same two altitude ranges. These results prove also the good performance of RALMO during daytime, although showing larger discrepancies than during nighttime, especially in the upper troposphere (from 5 to 10 km). The reliability and the high quality of the *T* profiles obtained by RALMO is a key aspect for addressing aerosol hygroscopic studies, since this is the most difficult to obtain of the atmospheric parameters using remote sensing techniques.

Figure 2 presents the same statistics than in the previous discussion but for *RH* measurements. As it was explained in Section 3, *RH* profiles from lidar were obtained from the combination of *r* and *T* measurements. Figure 2a shows all *RH* deviation profiles between lidar and RS while Figure 2b presents the mean *RH* deviation profile. This plot reveals a small bias between both instruments that ranges from positive values (+3%RH at 1.4 km asl) to negatives (-9%RH at 5.6 km asl). Above 9 km (asl) the bias becomes again positive reaching a maximum value of +6%RH. The mean bias and standard deviation along the region from ground to 2.1 km asl is +2.0±0.9 %RH while it increases to -4±2 %RH in the range 2.1-9 km. We can affirm that the shape observed in the *RH* bias between both instruments is mainly coming from the *r* measurements since the *T* statistics showed a negligible bias in the whole column (with almost zero bias, not shown). It is due to larger inhomogeneities in *r* in time and in space which produces larger discrepancies between lidar and RS observations. Regarding the standard deviations observed for this parameter (Fig. 2c) we can observe that it increases with altitude in the lower troposphere (from 4.4%RH at ground to 8%RH at 2 km asl). Above this altitude the standard deviation values oscillate around a quite constant value in altitude. The mean *RH* standard deviation in the lower troposphere (from ground to 2.1 km) was 6.5±1.3%RH while it was 8.5±1.5%RH above this altitude. The *RH* comparison for daytime measurements (not shown here) also presented a small bias between lidar and RS, with a mean values of -0.4±2.4 %RH in the range from ground to 5 km asl. The mean standard deviations obtained for the same altitude range was slightly larger than during nighttime with a mean value of 9±3 %RH. Above 5 km (asl) and during daytime the SNR of RALMO is smaller compared to night-time measurements due to the solar background, for this reason the *RH* profiles were not calculated above this altitude in order to avoid large uncertainties. In any case we would like to highlight the good quality of RALMO *RH* information. The high quality of the *RH* measurements

shown in this intercomparison is a key aspect to be able to address the aerosol hygroscopic studies, as will be shown in the next sections.

5 Study of aerosol hygroscopicity

Two case studies are presented in which the hygroscopicity of different types of aerosol is characterized. The two case studies took place during summer 2017, and feature smoke particles and mineral dust.

5.1 Case I: hygroscopic growth of smoke mixture

Case I corresponds to 7th September 2017. The temporal evolution of *r*, *RH* and β^{aer} at 355 nm in the lower troposphere (0-5 km asl) is shown in Fig. 3 for this day. According to the aerosol measurements (lowest panel), low clouds were present at around 1.6 km (agl) during the first part of the day (until 12 UTC). After that, two clear aerosol layers can be identified, the Atmospheric Boundary Layer (ABL) and a strong lofted aerosol layer located between 2 and 4 km (agl) which appeared in the afternoon. A usual convective boundary layer development was observed during the day with maximum height occurring at around 14:00 UTC. It is interesting to remark how within the ABL the intensity of the aerosol backscatter signal was stronger at the top of this layer even when a strong mixing was expected at the central hours of the day (between 13:00 and 17:00 UTC). However, a larger homogeneity was observed for the same layer in the *r* measurements (Fig. 3, upper panel), indicating that the convective processes were strong enough to produce a well mixed ABL in that time interval. The third element, that can help to understand the observed variations in the backscatter signals is the *RH* measurements (central panel). From that plot, we can observe how the intensification observed in β^{aer} is well correlated with the values observed for *RH*, with the highest values of both properties at the top of the ABL. This kind of behaviour could be due to aerosol hygroscopic processes and a detailed analysis is presented in the following paragraphs.

According to the NAAPS (Navy Aerosol Analysis and Prediction System) (Christensen, 1997) model, 7th September 2017 at 18:00 UTC is characterized by the presence of smoke above the measurement station (Fig. 4a). This model predicted smoke surface concentrations (blue colour map) between 4 and 8 $\mu g/m^3$ at Payerne. The Hysplit backtrajectories analysis indicated that the air masses above our station in the lower layers of the troposphere had their origin in North America (Fig. 4b). The VIIRS (Visible Infrared Imaging Radiometer Suite) fire and thermal anomalies product available from the joint NASA/NOAA Suomi-National Polar orbiting Partnership (S-NPP) satellite (Fig. 4c), showed that in the studied period (from 25th August to 3rd September of 2017) several intensive hot spots were found along the calculated air mass trajectories, especially in some areas of Northwest of the United States and in the central part of Canada. In addition, Carbon Monoxide (CO) observations from the Atmospheric Infrared Sounder (AIRS) on board of Aqua satellite monitored a plume (not shown here) with high concentration of CO that moved from North America to Europe during that period, reaching the Eastern part of Europe on 6th September 2017. Over Payerne, the total column CO concentrations observed with AIRS were in the range of 100 and 130 parts per billion by volume (ppbv) during 7th and 8th September, which are considerably higher than the mean concentration

observed in the previous month (70-80 ppbv). CO is considered a good tracer of smoke particles since it is generated in the incomplete combustion of biomass.

In-situ measurements carried out at Payerne station showed some changes in the aerosol properties that could be characteristics of smoke particles (Fig. 5). An increase in the PM2.5 mass concentration was observed in the period from 6th to 8th of September with values changing from 1 $\mu g/m^3$ (12 UTC on 6th September) to 9.9 $\mu g/m^3$ (20 UTC on 8th September), indicating an increase in the concentration of small particles at the surface. The PM2.5 concentration reached during that evening was clearly above the mean summer value (5.2 $\mu g/m^3$). The PM2.5 increase occured at the same time of an increase of the absorption coefficient at different wavelengths observed by an aethalometer. The absorption Angstrom exponent (AAE), which represents the wavelength dependence of absorption and depends on the composition of absorbing aerosols showed relatively low values (between 1.1 and 1.3 for most of the measurements) which can be characteristics of biomass burning particles (Schmeisser et al., 2017). Therefore, model predictions and satellite and in-situ observations agreed and point to a mixture of local aerosol and smoke particles from biomass burning in the atmospheric column over Payerne.

Vertical information of aerosol, *T* and *r* was obtained using the RALMO lidar and ceilometer measurements on 7th September 2017. Figure 6 shows the profiles of β^{aer} at 355 nm and 1064 nm, *RH* and the auxiliary information of θ and *r* for the time interval 15:00-15:30 UTC. From this figure, a marked increase of β^{aer} with altitude was observed for the altitude range between 1.7 and 2.3 km (asl). Simultaneously to this increase, we observed an increase in *RH* with values increasing from 73% (bottom of the layer) to 97% (top of the layer). The profiles of θ and *r* (Fig. 6c) were used as indicators of a good mixing as explained in section 3.2. These profiles show quite constant values for both properties within the layer (300.6 $\pm$ 0.5 K and 5.3 $\pm$ 0.1 g/kg, respectively), indicating that the layer was well mixed.

Following the methodology presented in Sect. 3.2 f_β at 355 and 1064 nm were obtained for the investigated layer from the combination of β^{aer} and *RH* measurements. Fig. 7 shows the dependency of $f_\beta(RH)$ with *RH*, called humidogram. The reference *RH* for this case was 73% which corresponds to the lowest value in the layer. From this figure, we can observe how β_{355} increased by a factor of 2.8 ($f_\beta(97\%)$=2.8) while humidity increased from 73% to 97% (blue points). Lower values of f_β are observed at 1064 nm (red points). In the infrared β increased by a factor of 1.8 with respect to its value at RH_{ref} (73%), indicating a lower sensitivity of this wavelength to the aerosol hygroscopic growth. Hänel hygroscopic parameters (γ) obtained using the fitting equation 7 were calculated (solid lines) in order to make our measurements comparable with other studies. This parameter is proportional to the aerosol hygroscopicity and it had values of 0.48$\pm$0.08 at 355 nm and 0.29$\pm$0.08 at 1064 nm. Independent vertical profiles obtained from the measurements of the previous 30-min time interval (from 14:30 to 15:00 UTC) were also analyzed in order to check the consistency of our results (figure not shown here). For that period, a simultaneous increase of β^{aer} and *RH* was also observed in the altitude range 1.5-2.2 km. Although the *RH* range observed for this time interval (70-93%) was slightly different from the one showed in Fig. 6, γ showed consistent results, within the associated uncertainties, for both time intervals ($\gamma_{355} = 0.57 \pm 0.14$ and $\gamma_{1064} = 0.35 \pm 0.14$). Similar value of hygroscopic parameter at 355 nm ($\gamma_{355} = 0.40$) is reported by Bedoya-Velásquez et al. (2018) associated with the presence of smoke particles. In that study a combination of lidar and MWR measurements was used for the aerosol hygroscopic analysis. However, the spectral dependency found in our case is not what has been reported in other studies. Higher values for longer wavelengths (between

355 and 532 nm) were found in γ in other studies for smoke particles and also for anthropogenic particles using remote sensing (Bedoya-Velásquez et al., 2018; Lv et al., 2017). Haarig et al. (2017) also reported this higher hygroscopicity at 1064 nm but for marine particles. In-situ studies also showed higher values for longer wavelengths although over a shorter range (450 - 700 nm) and for marine particles (Kotchenruther et al., 1999; Zieger et al., 2013).

We performed Mie simulations in order to understand if the spectral dependency observed in our study could be realistic or not. β^{aer} at the lidar wavelengths (355, 532 and 1064 nm) as a function of *RH* were computed using a Mie code (Bond et al., 2006; Mätzler, 2002). For these simulations some inputs such as the aerosol growth factor (1.6 which is typical for hygroscopic aerosol) and the refractive index (m = 1.5 + i0.01) were assumed. Figure 8 shows the f_β calculated from the Mie calculation as a function of *RH* for different wavelengths and particle sizes. Monomodal distributions were used assuming different diameters for the dry particles and a geometric standard deviation of 1.5. From this figure we can observe that the backscatter is very sensitive to wavelength and particle size as expected, whose relationship is characterized in scattering theory by the size parameter ($x = \pi D/\lambda$) where D is particle diameter. Mie scattering regime is expected for x$\approx$1. A stronger increase in the backscattered radiation at the shortest wavelengths is expected for small particles (D_{dry}=200 nm) when *RH* increases according to these simulations (Fig. 8a). These results indicate that even a decrease in β^{aer} at 1064 nm could be expected when the size particle increase due to hygroscopic growth. Figure 8b shows the humidogram for a dry particle diameter of 400 nm. A different spectral dependency is observed for this case with slightly higher f_β at 532 nm than at 355 nm and lower at 1064 nm. These results agree with our observations and also explain the different spectral dependency observed in other studies for smoke and anthropogenic particles that could have similar sizes (small particles) to what is simulated here. Panels c and d in Figure 8 show that for the biggest dry particle diameters (600 and 800 nm) the spectral dependency of f_β is inverted with respect to small particles with larger f_β values at the longest wavelengths. This spectral dependency agrees with the observations in Haarig et al. (2017) for marine particles which are considered much bigger particles than smoke particles. However, we must also point out that for many cases, larger particles in the atmosphere are further away from the ideal case of a sphere considered in Mie theory. Hence, this type of comparison should be considered with caution.

Continuous aerosol and *RH* measurements from RALMO lidar also allows to monitor aerosol hygroscopic processes occurring in time. Figure 9 shows the evolution of *r*, wind direction, β^{aer} at 355 nm and *RH* at 1.3 km (asl) on 7th September 2017. As it was indicated in Section 3.2, water vapour is considered a good tracer in the atmosphere and constant values of *r* mean the air parcels have very similar origins. In this case, we can observe that *r* was quite constant (6.7$\pm$0.3 g/kg, Fig. 9, top) during the evening (from 16:00 to 23:30 UTC), fulfilling the previous criterion. In addition, a simultaneous increase of β^{aer} and *RH* was observed for the indicated period and altitude (Fig. 9, bottom). *RH* changed from 63% in late afternoon to reach values close to 90% at midnight.

In order to quantify the aerosol hygroscopic effect that took place in time, f_β was calculated for these measurements (Fig. 10a, blue filled circles). The initial value of β^{aer}_{355} (at $RH_{ref} = 63\%$) increased by a factor of 2 when *RH* reached the maximum values of the evening. The Hänel parameterization was used for this dataset providing a hygroscopic parameter of 0.54$\pm$0.17 which is in good agreement with the values observed in the atmospheric column in the afternoon of this day. In addition to this hydration process (water uptake) we could also observe the dehydration (evaporation) that occurred within this aerosol layer

during the afternoon of this day (from 11:00 to 16:00 UTC, Fig. 9). In this period, *r* and the wind direction measurements were stable (6.0±0.5 g/kg and 302°± 27°, respectively), evidence that the air mass did not change. A decrease of β_{355}^{aer} took place at the same time when *RH* decreased from 93% to 59%. The humidogram obtained for this dehydration process (Fig. 10a, blue open circles) also showed f_β values very close to the ones calculated in the later period and a hygroscopic parameter from Hänel parametrization of 0.40±0.08. The same behaviour was observed for β_{1064} from the ceilometer measurements along this day, with hygroscopic parameter values of 0.41±0.16 and 0.34±0.09 for hydration and dehydration processes, respectively, showing again lower values than at the ultraviolet channel. We would like to remark the good agreement found in the aerosol hygroscopicity of this case using a vertical and a temporal analysis.

5.2 Case II: hygroscopic growth of mineral dust particles

The second case took place on 8th July 2017. Figure 11 shows the evolution of *r*, *RH* and β^{aer} at 355 nm from RALMO during the morning of this day. From the aerosol measurements (lowest panel) the presence of particles at high altitudes is evident, reaching almost 6 km (asl) in the late morning (around 9 UTC). For this day, the NMMB/BSC (Non-hydrostatic Multiscale Model/Barcelona Supercomputing Center) Dust model (Pérez et al., 2011) predicted dust particles over the western part of Europe, including Switzerland. A dust concentration profile calculated using this model for the Earlinet station of Payerne (Fig. 12a) showed higher concentration of mineral dust in the lower troposphere with a profile very similar to what was observed with our Raman lidar (Fig. 12b). Back-trajectories analysis from HYSPLIT model (not shown here) indicated that the observed air masses had their origin in North Africa. Remote and in-situ measurements carried out at our station also confirmed features typical of this kind of particles. AOD Angstrom exponent obtained from the PFR sun-photometer measurements presented low values (between 0.5 and 0.6) throughout the morning, indicating the presence of coarse particles in the atmospheric column. In-situ measurements also showed a strong increase in the PM10 concentration at the surface during this day with values ranging from 14 μg/m^3 at 03:00 UTC to 37.4 μg/m^3 at 15:00 UTC. The annual mean PM10 concentration in 2017 was 12 μg/m^3 which is much lower than the values observed during this event.

Once the aerosol was well identified using models and measurements, we analyzed the vertical profiles obtained from the lidar (Fig. 13, a-c). We observed a simultaneous increase of β^{aer} from the lidar systems with *RH* at the altitude range between 1.9 and 2.3 km (asl). For that range, *r* and θ showed quite constant values, evidence of a well mixed layer. The dependence of f_β at 355 and 1064 nm with *RH* is shown in the resultant humidogram in Fig. 13d. Although there was an intensification of the backscatter in both wavelengths ($f_\beta^{355}(84\%) = 1.2$ and $f_\beta^{1064}(84\%) = 1.1$ with $RH_{ref} = 68\%$), it was much lower compared to case I. The hygroscopic parameter obtained from the Hänel parametrization confirmed this behaviour, with values of 0.20±0.18 and 0.12±0.19 at 355 and 1064 nm, respectively. These values are similar to the ones observed by Lv et al. (2017) also under the presence of mineral dust ($\gamma_{355} = 0.12$ and $\gamma_{532} = 0.24$). As in Case I, we found the opposite spectral dependency compared to Lv et al. (2017). However, we considered a wider spectral range.

6 Evaluation of the effect of aerosol hygroscopicity on the Earth's radiative balance

Because of the changes in aerosol optical and microphysical properties due to water uptake, aerosol radiative properties are modified in case of hygroscopic growth. As stated before, aerosol backscatter and extinction coefficients increase under high *RH* conditions which in turn leads to an increase of the AOD. To compute the AOD, the β^{aer} profiles at 355 nm were converted to extinction using a generic lidar ratio of 50 sr. Although the choice of LR could affect the AOD, the relative contribution due to aerosol hygroscopicity would remain almost constant. In order to calculate ΔAOD, the increment of AOD due to hygroscopic growth, we obtain a so-called "dry" aerosol extinction profile by using the Hänel parameterization and assuming that *RH* in the analyzed layer is equal to RH_{ref} for each case. The "dry" profiles obtained are included in Figure 14. AOD for the dry and wet cases, as well as ΔAOD, are summarized in Table 1.

For the two cases analyzed here, the increase in AOD at 355 nm related to the hygroscopic growth in the analyzed layers is ΔAOD = 0.017 (with ΔAOD=AOD$-$AOD$_{dry}$) for Case I and ΔAOD = 0.001 for Case II. In relative terms, this results in an increase of the total AOD of 4.7% (15.6% if we consider only AOD in the ABL where the hygroscopic layer is located) due to hygroscopic growth for Case I, and 0.6% for Case II. As expected, ΔAOD is much larger in Case I since smoke particles are more hygroscopic (γ_{355} = 0.48) than mineral dust (γ_{355} = 0.20). It is worth noting the significant effect of the hygroscopic growth on the ABL AOD which increases nearly by 16%.

Simulations with a radiative transfer model can give us an estimate of the impact that this change in AOD has on the aerosol radiative effect (ARE). In this case, we use GAME (Global Atmospheric ModEl, Dubuisson et al. (1996, 2005)). GAME is a modular radiative transfer model that allows calculating upward and downward radiative fluxes at different vertical levels with high resolution by using the discrete ordinates method (Stamnes et al., 1988). Details about the model parameterization can be found in Sicard et al. (2014) and Granados-Muñoz et al. (2019). In our case, the variations in the ARE (ΔARE) in the shortwave spectral range are exclusively related to the variations in AOD and the AE due to hygroscopic growth, whereas the other aerosol properties are assumed to remain constant. The calculation was done for a solar zenith of 30° corresponding to Case I, which presented stronger hygroscopicity and occurred at daytime (15:00 UTC). The changes in AOD produce a net increase (in absolute and relative values) of the aerosol radiative effect at the surface with respect to the "dry" profiles equal to 2.4 Wm^{-2} (5.2%) and 0.1 Wm^{-2} (0.4%) in Case I and Case II, respectively. The interpretation of these results needs to be done carefully. Even though radiative transfer models do not provide an estimation of the ARE uncertainties, a sensitivity test performed in Granados-Muñoz et al. (2019) showed that an uncertainty in the AOD of 0.05 can lead to uncertainties in the ARE of up to 30%. The values of ΔARE obtained here are certainly within this uncertainty limits and an accurate quantitative estimation of the hygroscopicity contribution to the ARE is quite complex. However it is necessary to highlight that our focus here is on the relative contribution of hygroscopic aerosol to the ARE when compared to dry conditions. As expected, the effect observed in our simulations is more noticeable in case of particles with stronger hygroscopic properties, such as the smoke mixture in Case I. We also note that the relative increase of AOD (4.7%) and ARE (5.2%) are similar. For the mineral dust event the effect is almost negligible (ΔARE=0.4%). Variations of the ARE observed in previous studies can reach up to 7 Wm^{-2} (Stock et al., 2011), however a comparison with our data is not straightforward since these variations are highly

dependent on the aerosol load and the aerosol type present in the atmosphere. In Case I, although the hygroscopic growth affects only a thin layer (only 600 m width) and the γ values are relatively low (0.48), the aerosol hygroscopic growth effect on the ARE is still quite noticeable. These results point out that in more favorable conditions, namely thicker layers where the hygroscopic effect occur and particles with stronger hygroscopic properties, the aerosol hygroscopic effect on the optical and radiative properties could be quite considerable. Therefore, we can conclude that including aerosol hygroscopic properties in climate model calculations is key for improving the accuracy of aerosol forcing estimates.

7 Conclusions

The present study demonstrates the capability of a Raman lidar to detect aerosol hygroscopic processes. Continuous measurements of water vapour, *T* and aerosol profiles are performed by RALMO lidar almost continuously since 2008 at the aerological station of MeteoSwiss in Payerne (Switzerland). These measurements allow us to monitor any change in aerosol properties that could occur as result of water uptake by particles under high *RH* (aerosol hygroscopic growth). To ensure that the changes in aerosol are only due to hygroscopic growth, several criteria were established. As first condition an increase in β^{aer} should occur simultaneously with an increase in *RH*. In addition, a high degree of homogeneity is required in the investigated layer. For that, backtrajectory analysis is used to verify that the origin of the air mass is independent of the altitude and low-varying or constant values of *r* and θ are required as proxy for well-mixed conditions throughout the aerosol layer.

The accuracy and the precision of RALMO *T* and *RH* profiles were assessed using collocated RS profiles. A total of 172 profiles were used in this intercomparison during day- and night-time for the period from July to December of 2017. The mean *T* deviations calculated from night-time (day-time) measurements revealed almost no bias between both techniques in the whole troposphere, with mean *T* deviations of 0.05$\pm$0.06 K (-0.5$\pm$0.2 K) in the first 5 km and 0.15$\pm$0.15 K (-0.1$\pm$0.6 K) above that altitude. The standard deviations also confirmed the excellent performance of RALMO with values below 1 K throughout the troposphere during nighttime and slightly larger values during daytime (0.8$\pm$0.2 K from ground to 5 km and 2.4$\pm$0.8 K from 5 to 10 km).

Lidar profiles of *RH* were obtained combining *r* and *T* measurements. Small *RH* biases were observed between both techniques during nighttime in the troposphere (from ground to 9 km asl) with values ranging between 3$\%RH$ at 1.4 km (asl) and -9$\%RH$ at 5.6 km (asl). The standard deviation of *RH* deviations also showed the good precision of the lidar measurements with values always lower than 9$\%RH$. The performance of RALMO in terms of *RH* during daytime in the lower troposphere (from ground to 5 km) were very similar to the ones obtained during nighttime. However, above 5 km the errors were much larger due to the solar background radiation and *RH* profiles were not calculated to avoid these large uncertainties. The good quality of the *RH* measurements found in this intercomparison is a key aspect to be able to address the aerosol hygroscopic studies.

The methodology presented here was applied to two case studies. In-situ and satellite measurements in addition to models indicate that Case I (7th September 2017) was characterized by a mixture of local aerosol and smoke particles from fires in North America. f_β was found to be 2.8 at 355 nm and 1.8 at 1064 when *RH* increased from 73 $\%$ to 97$\%$ in the investigated

layer. The Hänel hygroscopic parameter which is proportional to the aerosol hygroscopicity took values of 0.48±0.08 at 355 nm and 0.29±0.08 at 1064 nm in this case. Independent vertical profiles obtained for a previous time interval showed the consistency of our results. Other remote sensing studies have shown a larger sensitivity to hygroscopic growth for longer wavelengths for this type of particles in contrast to our results. However, those studies were carried out in a shorter wavelength range (355-532 nm). Haarig et al. (2017) also observed a higher hygroscopicity at 1064 nm than at 355 nm but for marine particles which are larger and much more hygroscopic than in our case. Mie simulations carried out in this study revealed that the spectral dependency of f_β can change strongly depending on the particle size and the wavelength of the incident radiation supporting our results as well as the study of Haarig et al. (2017).

Continuous aerosol and *RH* measurements from RALMO also allowed monitoring aerosol hygroscopic processes as function of time for this first case. The evolution of β and *RH* at 1.3 km (asl) on 7th September 2017 showed two periods in which there was a simultaneous decrease of both parameters (dehydration process) followed by a simultaneous increase (hydration process). The Hännel hygroscopic parameters calculated from the humidogram (f_β vs. *RH*) for both periods took values of 0.54±0.17 (0.43±0.16) and 0.40±0.08 (0.34±0.09) at 355 nm (1064 nm) for the hydration and dehydration processes, respectively, which are in good agreement with the results obtained in the spatial (vertical) analysis.

The aerosol hygroscopicity of a second case (8th July 2017), characterized by the presence of dust particles, was also analyzed in this study. The spatial analysis of the lidar measurements revealed also hygroscopic growth for these particles but with a very different behaviour. A much lower hygroscopicity than for the previous case (smoke mixture) was observed with β increasing only 1.2 and 1.1 times at 355 and 1064 nm, respectively, when *RH* increased from 68% to 84%. The hygroscopic parameters obtained from the humidogram were 0.20±0.18 and 0.12±0.19 at 355 and 1064 nm, respectively, showing a good agreement with values observed in other studies for mineral dust. The lower spectral sensitivity to the aerosol hygroscopicity found for this type of particles was also remarkable.

Finally, the impact of aerosol hygroscopicity on the Earth's radiative balance was evaluated for the two presented cases using a radiative transfer model (GAME). The aerosol hygroscopic growth in the investigated layers produced an increase in AOD at 355 nm of 0.017 (4.7%) for the case with presence of smoke particles and 0.001 (0.6%) for the case with mineral dust. These changes in AOD produced a net increase in absolute (and relative) values of the radiative effect at the surface of 2.4 Wm^{-2} (5.2%) and 0.1 Wm^{-2} (0.4%) in Case I and Case II, respectively. The results were significant for the case with presence of smoke particles (more hygroscopic) despite the aerosol load of the investigated layer not having been very high. Therefore, we conclude that the effect of aerosol hygroscopicity on optical and radiative properties is important and has to be considered in climate model calculations to improve aerosol forcing estimates.

In future work we want to exploit the large data set (10 years) of simultaneous aerosol and *RH* profiles from this Raman lidar to carry out a statistical analysis of aerosol hygroscopic properties.

Data availability. Data used in this paper are available upon request from corresponding author (francisco.navas@meteoswiss.ch).

Competing interests. The authors declare that they have no conflict of interest.

Author contributions. FNG designed the experiment, analyzed the data and wrote the manuscript, GM worked on the T retrievals, MH and MCC performed the Mie simulations, AH is responsible for the lidar measurements and participed in the numerous scientific discussions and MJGR and MS performed the calculations with the radiative transfer model (GAME). All authors provided comments on the manuscript.

Acknowledgements. This work was supported by the Swiss National Science Foundation trough project PZ00P2 168114. We thank to EMPA and the Swiss Federal Office for the Environment (FOEN) for providing the data of the in-situ measurements carried out at Payerne within the Nabel monitoring program. We also acknowledge the financial support by the European Union's Horizon 2020 research and innovation program through project ACTRIS-2 (grant agreement no. 654109). The radiative transfer simulations performed with GAME are supported by the European Union GRASP-ACE MSCA-RISE Action (grant agreement no. 778349); the Spanish Ministry of Economy and Competitiveness (ref. TEC2015-63832-P) and EFRD (European Fund for Regional Development); the Spanish Ministry of Science, Innovation and Universities (ref. CGL2017-90884-REDT); the Unity of Excellence Maria de Maeztu (ref. MDM-2016-0600) financed by the Spanish Agencia Estatal de Investigación. This work was also supported by the Juan de la Cierva-Formación program (grant FJCI-2015-23904). The authors also kindly acknowledge Philippe Dubuisson (Laboratoire d'Optique Atmosphérique, Université de Lille, France) for the use of the GAME model.

References

Ansmann, A., Riebesell, M., Wandinger, U., Weitkamp, C., Voss, E., Lahmann, W., and Michaelis, W.: Combined Raman elastic-backscatter lidar for vertical profiling of moisture, aerosol extinction, backscatter, and lidar ratio, Applied Physics B, 55, 18–28, 1992.

Bedoya-Velásquez, A., Navas-Guzmán, F., Granados-Muñoz, M., Titos, G., Román, R., Andrés Casquero-Vera, J., Ortiz-Amezcua, P., Antonio Benavent-Oltra, J., De Arruda Moreira, G., Montilla-Rosero, E., Hoyos, C., Artiñano, B., Coz, E., Olmo-Reyes, F., Alados-Arboledas, L., and Guerrero-Rascado, J.: Hygroscopic growth study in the framework of EARLINET during the SLOPE i campaign: Synergy of remote sensing and in situ instrumentation, Atmospheric Chemistry and Physics, 18, https://doi.org/10.5194/acp-18-7001-2018, 2018.

Bindoff, N., Stott, P., AchutaRao, K., Allen, M., Gillett, N., Gutzler, D., Hansingo, K., Hegerl, G., Hu, Y., Jain, S., Mokhov, I., Overland, J., Perlwitz, J., Sebbari, R., and Zhang, X.: Detection and Attribution of Climate Change: from Global to Regional. In: Climate Change 2013: The Physical Science Basis. Contribution of Working Group I to the Fifth Assessment Report of the Intergovernmental Panel on Climate Change [Stocker, T.F., D. Qin, G.-K. Plattner, M. Tignor, S.K. Allen, J. Boschung, A. Nauels, Y. Xia, V. Bex and P.M. Midgley (eds.)], Cambridge University Press, Cambridge, United Kingdom and New York, NY, USA., pp. 867–952, 2013.

Bond, T. C., Habib, G., and Bergstrom, R. W.: Limitations in the enhancement of visible light absorption due to mixing state, Journal of Geophysical Research: Atmospheres, 111, 2006.

Bösenberg, J., Matthias, V., Linné, H., Comerón Tejero, A., Rocadenbosch Burillo, F., Pérez López, C., and Baldasano Recio, J. M.: EARLINET: A European Aerosol Research Lidar Network to establish an aerosol climatology, Report. Max-Planck-Institut fur Meteorologie, pp. 1–191, 2003.

Brocard, E., Philipona, R., Haefele, A., Romanens, G., Mueller, A., Ruffieux, D., Simeonov, V., and Calpini, B.: Raman Lidar for Meteorological Observations, RALMO-Part 2: Validation of water vapor measurements, Atmospheric Measurement Techniques, 6, 2013.

Christensen, J. H.: The Danish Eulerian hemispheric model—A three-dimensional air pollution model used for the Arctic, Atmospheric Environment, 31, 4169–4191, 1997.

Collaud Coen, M., Weingartner, E., Schaub, D., Hueglin, C., Corrigan, C., Henning, S., Schwikowski, M., and Baltensperger, U.: Saharan dust events at the Jungfraujoch: detection by wavelength dependence of the single scattering albedo and first climatology analysis, Atmospheric Chemistry and Physics, 4, 2465–2480, 2004.

Dinoev, T., Simeonov, V., Arshinov, Y., Bobrovnikov, S., Ristori, P., Calpini, B., Parlange, M., and Van den Bergh, H.: Raman Lidar for Meteorological Observations, RALMO-Part 1: Instrument description, Atmospheric Measurement Techniques, 6, 1329–1346, 2013.

Draxler, R. R. and Rolph, G. D.: HYSPLIT (HYbrid Single-Particle Lagrangian Integrated Trajectory) model access via NOAA ARL READY website (http://ready.arl.noaa.gov/HYSPLIT.php), NOAA Air Resources Laboratory, Silver Spring, 2003.

Dubuisson, P., Buriez, J., and Fouquart, Y.: High spectral resolution solar radiative transfer in absorbing and scattering media: Application to the satellite simulation, Journal of Quantitative Spectroscopy and Radiative Transfer, 55, 103–126, 1996.

Dubuisson, P., Giraud, V., Chomette, O., Chepfer, H., and Pelon, J.: Fast radiative transfer modeling for infrared imaging radiometry, Journal of Quantitative Spectroscopy and Radiative Transfer, 95, 201–220, 2005.

Feingold, G. and Morley, B.: Aerosol hygroscopic properties as measured by lidar and comparison with in situ measurements, Journal of Geophysical Research: Atmospheres, 108, 2003.

Fernández, A., Molero, F., Becerril-Valle, M., Coz, E., Salvador, P., Artíñano, B., and Pujadas, M.: Application of remote sensing techniques to study aerosol water vapour uptake in a real atmosphere, Atmospheric Research, 202, 112–127, 2018.

Fierz-Schmidhauser, R., Zieger, P., Gysel, M., Kammermann, L., DeCarlo, P., Baltensperger, U., and Weingartner, E.: Measured and predicted aerosol light scattering enhancement factors at the high alpine site Jungfraujoch, Atmospheric Chemistry and Physics, 10, 2319–2333, 2010.

Goldsmith, J., Blair, F. H., Bisson, S. E., and Turner, D. D.: Turn-key Raman lidar for profiling atmospheric water vapor, clouds, and aerosols, Applied Optics, 37, 4979–4990, 1998.

Granados-Muñoz, M., Guerrero-Rascado, J., Bravo-Aranda, J., Navas-Guzmán, F., Valenzuela, A., Lyamani, H., Chaikovsky, A., Wandinger, U., Ansmann, A., Dubovik, O., et al.: Retrieving aerosol microphysical properties by Lidar-Radiometer Inversion Code (LIRIC) for different aerosol types, Journal of Geophysical Research: Atmospheres, 119, 4836–4858, 2014.

Granados-Muñoz, M. J., Navas-Guzmán, F., Bravo-Aranda, J. A., Guerrero-Rascado, J. L., Lyamani, H., Valenzuela, A., Titos, G., Fernández-Gálvez, J., and Alados-Arboledas, L.: Hygroscopic growth of atmospheric aerosol particles based on active remote sensing and radiosounding measurements: selected cases in southeastern Spain, Atmospheric Measurement Techniques, 8, 705–718, 2015.

Granados-Muñoz, M. J., Sicard, M., Román, R., Benavent-Oltra, J. A., Barragán, R., Brogniez, G., Denjean, C., Mallet, M., Formenti, P., Torres, B., et al.: Impact of mineral dust on shortwave and longwave radiation: evaluation of different vertically resolved parameterizations in 1-D radiative transfer computations, Atmospheric Chemistry and Physics, 19, 523–542, 2019.

Haarig, M., Ansmann, A., Gasteiger, J., Kandler, K., Althausen, D., Baars, H., Radenz, M., and Farrell, D. A.: Dry versus wet marine particle optical properties: RH dependence of depolarization ratio, backscatter, and extinction from multiwavelength lidar measurements during SALTRACE, Atmospheric Chemistry and Physics, 17, 14 199, 2017.

Haeffelin, M., Laffineur, Q., Bravo-Aranda, J. A., Drouin, M. A., Casquero-Vera, J. A., Dupont, J. C., and Backer, H. D.: Radiation fog formation alerts using attenuated backscatter power from automatic lidars and ceilometers, Atmospheric Measurement Techniques, 9, 5347–5365, 2016.

Hänel, G.: The properties of atmospheric aerosol particles as functions of the relative humidity at thermodynamic equilibrium with the surrounding moist air, in: Advances in geophysics, vol. 19, pp. 73–188, Elsevier, 1976.

Haywood, J. and Boucher, O.: Estimates of the direct and indirect radiative forcing due to tropospheric aerosols: A review, Reviews of geophysics, 38, 513–543, 2000.

Klett, J. D.: Stable analytical inversion solution for processing lidar returns, Applied optics, 20, 211–220, 1981.

Kotchenruther, R. A., Hobbs, P. V., and Hegg, D. A.: Humidification factors for atmospheric aerosols off the mid-Atlantic coast of the United States, Journal of Geophysical Research: Atmospheres, 104, 2239–2251, 1999.

List, R.: Smithsonian Meteorological Tables, 6th rev. ed., Washington, DC, 1951.

Lv, M., Liu, D., Li, Z., Mao, J., Sun, Y., Wang, Z., Wang, Y., and Xie, C.: Hygroscopic growth of atmospheric aerosol particles based on lidar, radiosonde, and in situ measurements: case studies from the Xinzhou field campaign, Journal of Quantitative Spectroscopy and Radiative Transfer, 188, 60–70, 2017.

Martucci, G., Voirin, J., Simeonov, V., Renaud, L., and Haefele, A.: A novel automatic calibration system for water vapor Raman LIDAR, in: EPJ Web of Conferences, vol. 176, p. 05008, EDP Sciences, 2018.

Martucci, G., Navas-Guzmán, F., Simeonov, V., Ludovic, R., and Haefele, A.: Validation of one-year of temperature data by the RAman Lidar for Meteorological Observations (RALMO) at Payerne, Atmospheric Measurement Techniques, in preparation.

Mätzler, C.: MATLAB Functions for Mie Scattering and Absorption-Research Report No 2002-08, Institut für Angewandte Physik: Bern, 2002.

McArthur, L., Halliwell, D. H., Niebergall, O. J., O'Neill, N. T., Slusser, J. R., and Wehrli, C.: Field comparison of network Sun photometers, Journal of Geophysical Research: Atmospheres, 108, 2003.

Muñoz-Porcar, C., Comerón, A., Sicard, M., Barragan, R., Garcia-Vizcaino, D., Rodríguez-Gómez, A., Rocadenbosch, F., and Granados-Muñoz, M. J.: Calibration of Raman Lidar Water Vapor Mixing Ratio Measurements Using Zenithal Measurements of Diffuse Sunlight and a Radiative Transfer Model, IEEE Transactions on Geoscience and Remote Sensing, pp. 1–10, 2018.

Navas-Guzmán, F., Bravo-Aranda, J. A., Guerrero-Rascado, J. L., Granados-Muñoz, M. J., and Alados-Arboledas, L.: Statistical analysis of aerosol optical properties retrieved by Raman lidar over Southeastern Spain, Tellus B: Chemical and Physical Meteorology, 65, 21 234, 2013.

Navas-Guzmán, F., Fernández-Gálvez, J., Granados-Muñoz, M. J., Guerrero-Rascado, J. L., Bravo-Aranda, J. A., and Alados-Arboledas, L.: Tropospheric water vapour and relative humidity profiles from lidar and microwave radiometry, Atmospheric Measurement Techniques, 7, 1201–1211, https://doi.org/10.5194/amt-7-1201-2014, 2014.

Navas-Guzmán, F., Kämpfer, N., and Haefele, A.: Validation of brightness and physical temperature from two scanning microwave radiometers in the 60 GHz O2 band using radiosonde measurements, Atmospheric Measurement Techniques (AMT), 9, 4587–4600, 2016.

Nyeki, S., Halios, C., Baum, W., Eleftheriadis, K., Flentje, H., Gröbner, J., Vuilleumier, L., and Wehrli, C.: Ground-based aerosol optical depth trends at three high-altitude sites in Switzerland and southern Germany from 1995 to 2010, Journal of Geophysical Research: Atmospheres, 117, 2012.

Pappalardo, G., Amodeo, A., Apituley, A., Comeron, A., Freudenthaler, V., Linné, H., Ansmann, A., Bösenberg, J., D'Amico, G., Mattis, I., et al.: EARLINET: towards an advanced sustainable European aerosol lidar network, Atmospheric Measurement Techniques, pp. 2389–2409, 2014.

Pérez, C., Haustein, K., Janjic, Z., Jorba, O., Huneeus, N., Baldasano, J., Black, T., Basart, S., Nickovic, S., Miller, R., et al.: Atmospheric dust modeling from meso to global scales with the online NMMB/BSC-Dust model–Part 1: Model description, annual simulations and evaluation, Atmospheric Chemistry and Physics, 11, 13 001–13 027, 2011.

Pilat, M. J. and Charlson, R. J.: Theoretical and optical studies of humidity effects on the size distribution of a hygroscopic aerosol, J. Rech. Atmos, 2, 166–170, 1966.

Sandradewi, J., Prévôt, A. S., Szidat, S., Perron, N., Alfarra, M. R., Lanz, V. A., Weingartner, E., and Baltensperger, U.: Using aerosol light absorption measurements for the quantitative determination of wood burning and traffic emission contributions to particulate matter, Environmental science & technology, 42, 3316–3323, 2008.

Schmeisser, L., Andrews, E., Ogren, J. A., Sheridan, P., Jefferson, A., Sharma, S., Kim, J. E., Sherman, J. P., Sorribas, M., Kalapov, I., et al.: Classifying aerosol type using in situ surface spectral aerosol optical properties, Atmospheric Chemistry and Physics, 17, 12 097–12 120, 2017.

Segura, S., Estellés, V., Titos Vela, G., Lyamani, H., Utrilla Navarro, P., Zotter, P., Prévôt, A., Močnik, G., Alados-Arboledas, L., and Martínez-Lozano, J.: Determination and analysis of in situ spectral aerosol optical properties by a multi-instrumental approach, 2014.

Sicard, M., Bertolín, S., Mallet, M., Dubuisson, P., and Comerón, A.: Estimation of mineral dust long-wave radiative forcing: sensitivity study to particle properties and application to real cases in the region of Barcelona, Atmospheric Chemistry and Physics, 14, 9213–9231, 2014.

Sicard, M., D'Amico, G., Comerón Tejero, A., Mona, L., Alados Arboledas, L., Amodeo, A., Baars, H., Baldasano Recio, J. M., Belegante, L., Binietoglou, I., et al.: EARLINET: potential operationality of a research network, Atmospheric measurement techniques, 8, 4587–4613, 2015.

Stamnes, K., Tsay, S.-C., Wiscombe, W., and Jayaweera, K.: Numerically stable algorithm for discrete-ordinate-method radiative transfer in multiple scattering and emitting layered media, Applied optics, 27, 2502–2509, 1988.

Stock, M., Cheng, Y., Birmili, W., Massling, A., Wehner, B., Müller, T., Leinert, S., Kalivitis, N., Mihalopoulos, N., and Wiedensohler, A.: Hygroscopic properties of atmospheric aerosol particles over the Eastern Mediterranean: implications for regional direct radiative forcing under clean and polluted conditions, Atmospheric Chemistry and Physics, 11, 4251–4271, 2011.

Swietlicki, E., Hansson, H.-C., Hämeri, K., Svenningsson, B., Massling, A., McFiggans, G., McMurry, P., Petäjä, T., Tunved, P., Gysel, M., et al.: Hygroscopic properties of submicrometer atmospheric aerosol particles measured with H-TDMA instruments in various environments—a review, Tellus B: Chemical and Physical Meteorology, 60, 432–469, 2008.

Titos, G., Cazorla, A., Zieger, P., Andrews, E., Lyamani, H., Granados-Muñoz, M. J., Olmo, F., and Alados-Arboledas, L.: Effect of hygroscopic growth on the aerosol light-scattering coefficient: A review of measurements, techniques and error sources, Atmospheric environment, 141, 494–507, 2016.

Vaughan, G., Wareing, D., Pepler, S., Thomas, L., and Mitev, V.: Atmospheric temperature measurements made by rotational Raman scattering, Applied Optics, 32, 2758–2764, 1993.

Veselovskii, I., Whiteman, D., Kolgotin, A., Andrews, E., and Korenskii, M.: Demonstration of aerosol property profiling by multiwavelength lidar under varying relative humidity conditions, Journal of Atmospheric and Oceanic Technology, 26, 1543–1557, 2009.

Whiteman, D. N.: Examination of the traditional Raman lidar technique. I. Evaluating the temperature-dependent lidar equations, Applied Optics, 42, 2571–2592, 2003a.

Whiteman, D. N.: Examination of the traditional Raman lidar technique. II. Evaluating the ratios for water vapor and aerosols, Applied optics, 42, 2593–2608, 2003b.

Wulfmeyer, V. and Feingold, G.: On the relationship between relative humidity and particle backscattering coefficient in the marine boundary layer determined with differential absorption lidar, Journal of Geophysical Research: Atmospheres, 105, 4729–4741, 2000.

Yau, M. K. and Rogers, R.: A short course in cloud physics, Elsevier, 1996.

Zhao, G., Zhao, C., Kuang, Y., Tao, J., Tan, W., Bian, Y., Li, J., and Li, C.: Impact of aerosol hygroscopic growth on retrieving aerosol extinction coefficient profiles from elastic-backscatter lidar signals, Atmospheric Chemistry and Physics, 17, 12 133–12 143, 2017.

Zieger, P., Fierz-Schmidhauser, R., Gysel, M., Ström, J., Henne, S., Yttri, K. E., Baltensperger, U., and Weingartner, E.: Effects of relative humidity on aerosol light scattering in the Arctic, Atmospheric Chemistry and Physics, 10, 3875–3890, 2010.

Zieger, P., Fierz-Schmidhauser, R., Weingartner, E., and Baltensperger, U.: Effects of relative humidity on aerosol light scattering: results from different European sites, Atmospheric Chemistry and Physics, 13, 10 609–10 631, 2013.

Table 1. Column AOD and ARE for both dry and wet conditions and their difference. All relative values are given with respect to the dry conditions.

	γ_{355}	Layer depth (m)	AOD_{355}	AOD_{355}^{dry}	ΔAOD_{355}	ARE (Wm^{-2})	ARE_{dry} (Wm^{-2})	ΔARE (Wm^{-2})
Case I (smoke)	0.48	600	0.379	0.362	0.017 (4.7%)	-48.8	-46.4	-2.4 (5.2%)
			0.126*	0.109*	0.017* (15.6%)*			
Case II (dust)	0.20	400	0.157	0.156	0.001 (0.6%)	-27.3	-27.2	-0.1 (0.4%)

*Indicates values within the ABL (between the surface and 2.5 km)

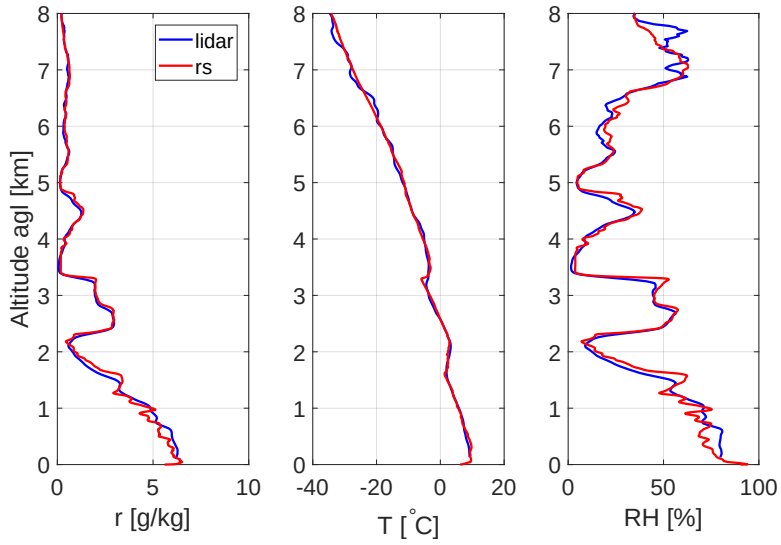

Figure 1. Mixing ratio (*r*), temperature (*T*) and relative humidity (*RH*) profiles from lidar (blue lines) and operational RS (red line) at 23:00 UTC on 20th September 2017.

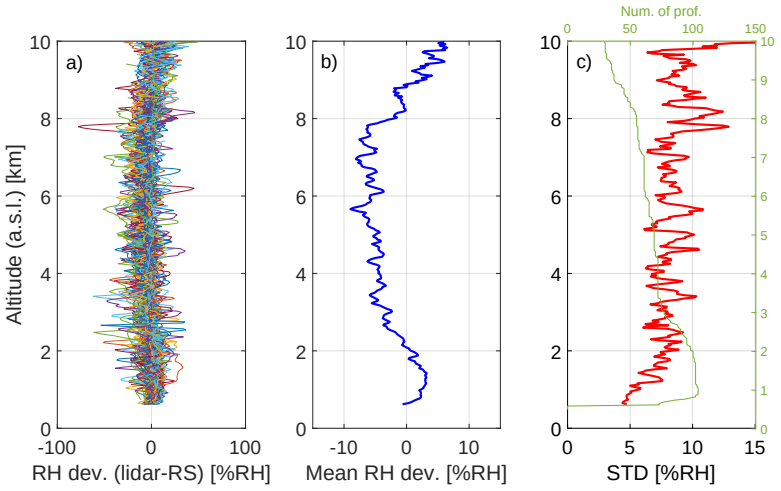

Figure 2. *RH* validation between RALMO lidar and RS at 23:00 UTC for the period from July to December 2017. (a) Profiles of *RH* deviation between lidar and RS. (b) Mean *RH* deviation (lidar-RS). (c) Standard *RH* deviation profile (red line) and number of profiles used at each altitude for this statistics (green line).

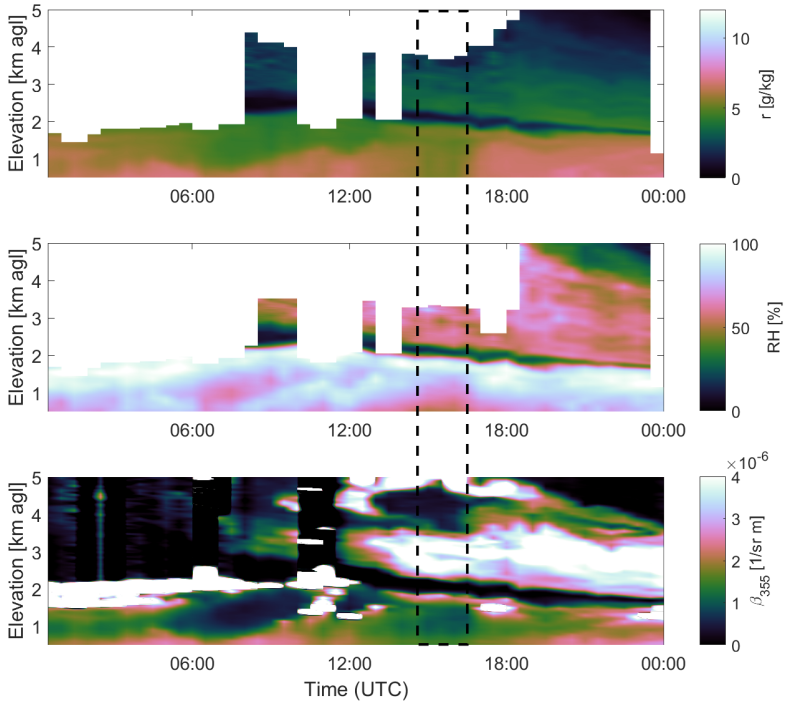

Figure 3. Temporal evolution of vertical profiles of *r*, *RH* and β^{aer} at 355 nm from RALMO lidar on 7th September 2017.

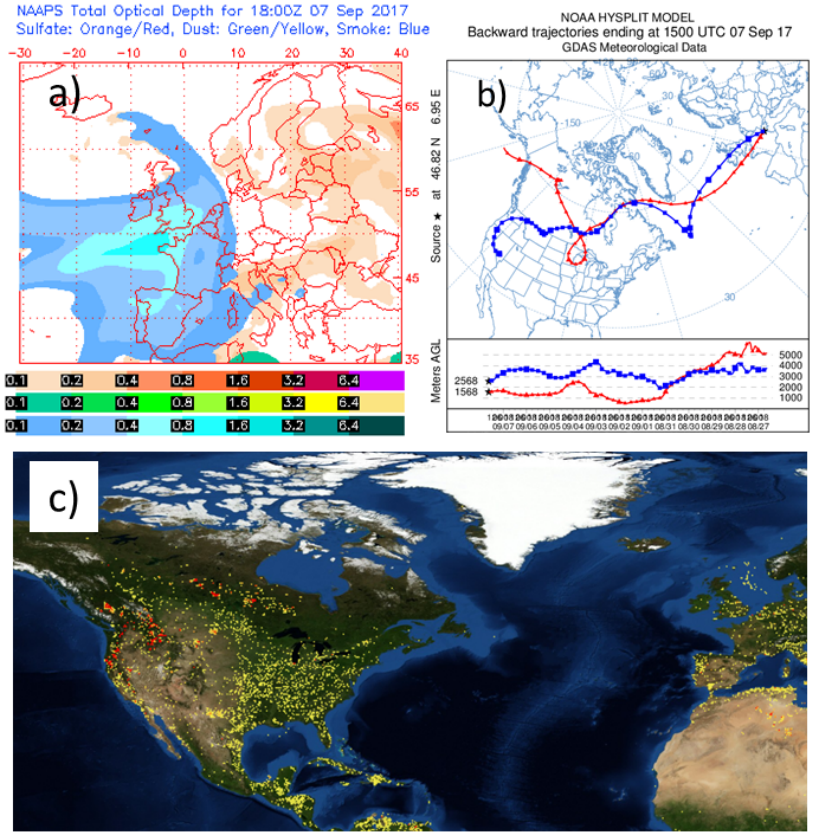

Figure 4. a) NAAPS total optical depth from sulfate (orange/red scale), dust (green/yellow scale) and smoke (blue scale) at 18 UTC on 7th September 2017. b) Backward trajectories from NOAA Hysplit model ending at 15 UTC 7 Sep 2017 calculated for the altitudes 2500 and 3500 m asl. c) Fire map from VIIRS instrument for the period from 25th August 2017 to 3rd September 2017.

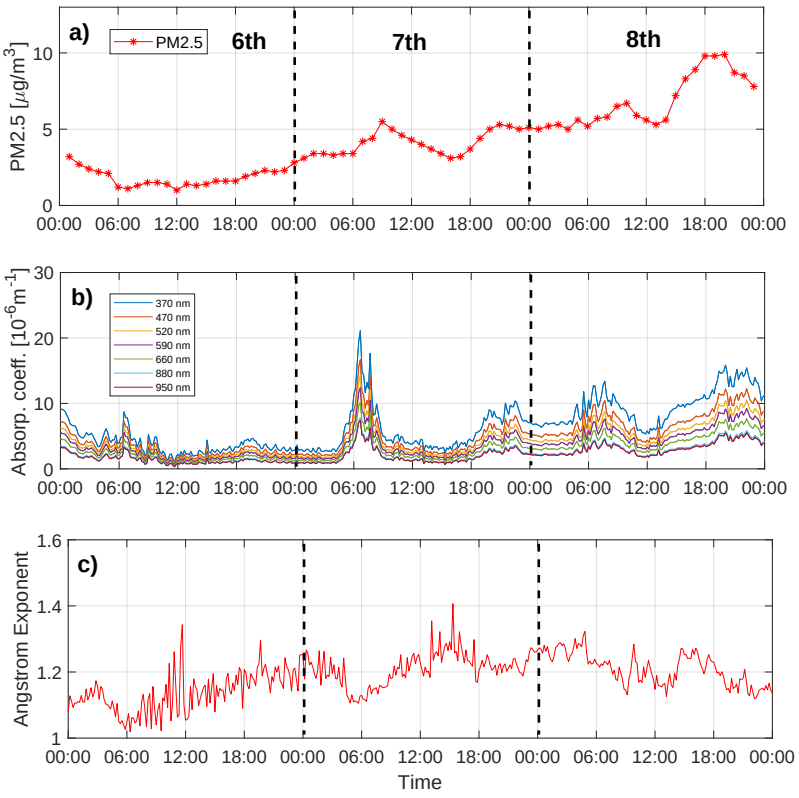

Figure 5. (a) Surface PM2.5 concentrations at Payerne from 6th to 8th of September 2017. (b) Absorption coefficient at 7 wavelengths and (c) absorption Angstrom exponent from aethalometer measurements.

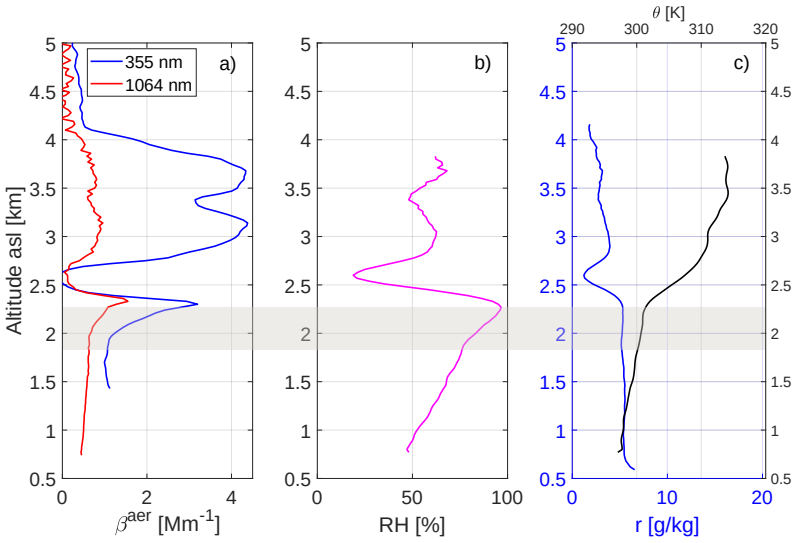

Figure 6. Vertical profiles of (a) β^{aer} at 355 and 1064 nm, (b) *RH* and (c) θ and r for the time interval 15:00-15:30 UTC on 7th September 2017. The grey shaded area indicates the layer in which aerosol hygroscopic growth occurred.

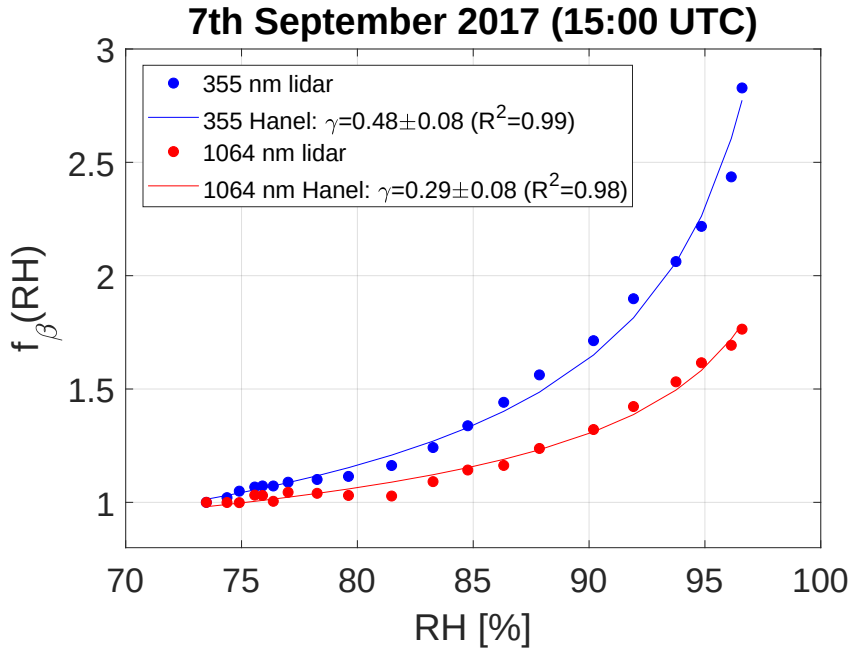

Figure 7. f_β at 355 and 1064 nm retrieved from the lidar profiles (layer: 1.7-2.3 km asl) at the time interval 15:00-15:30 UTC on 7th September 2017.

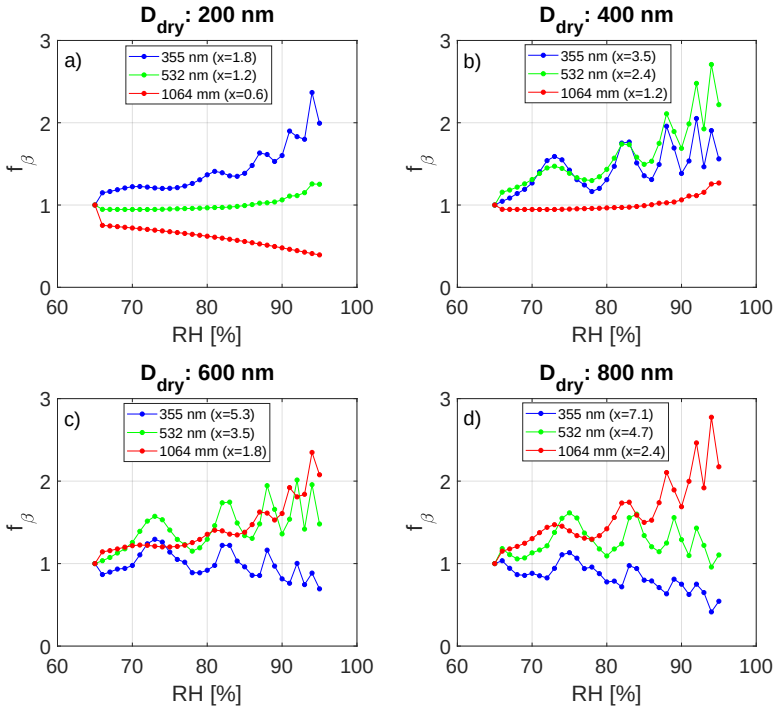

Figure 8. f_β calculated from Mie simulations at 355, 532 and 1064 nm and for different particle diameters.The size parameter (x) has been indicated for each configuration of wavelength and size particle.

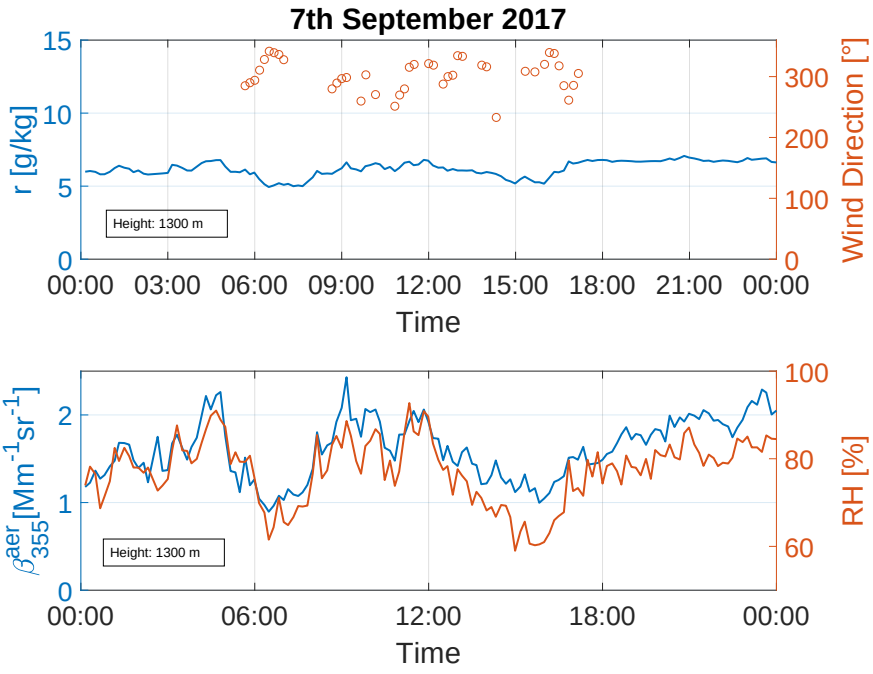

Figure 9. Evolution of *r* and wind direction (top panel) and β^{aer}_{355} and *RH* (bottom panel) at 1.3 km (asl) on 7th September 2017.

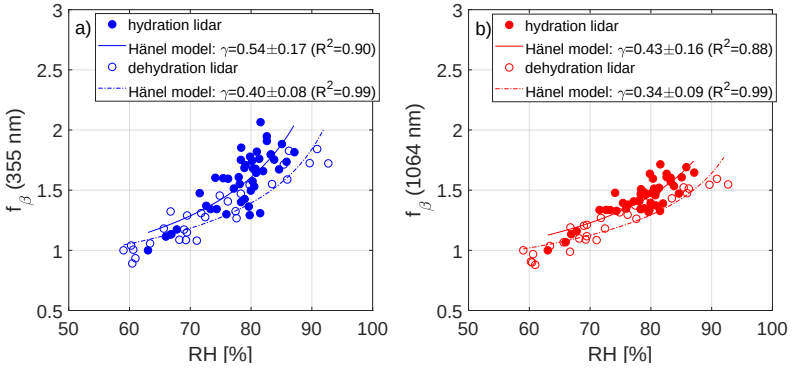

Figure 10. Humidograms at 355 nm (a) and 1064 nm (b) retrieved from continuous measurements for hydration and dehydration processes on 7th September 2017.

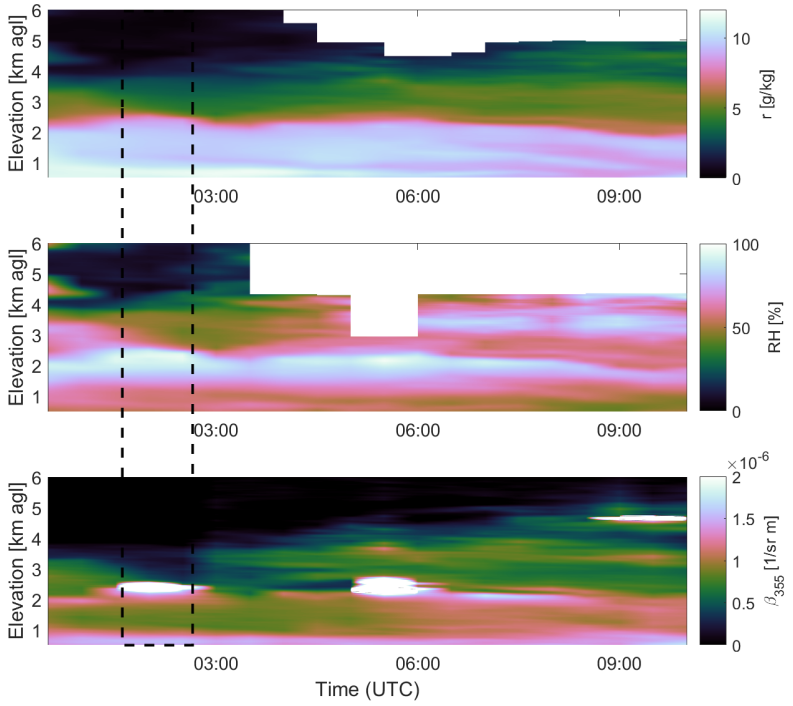

Figure 11. Same as figure 3, on 8th July 2017.

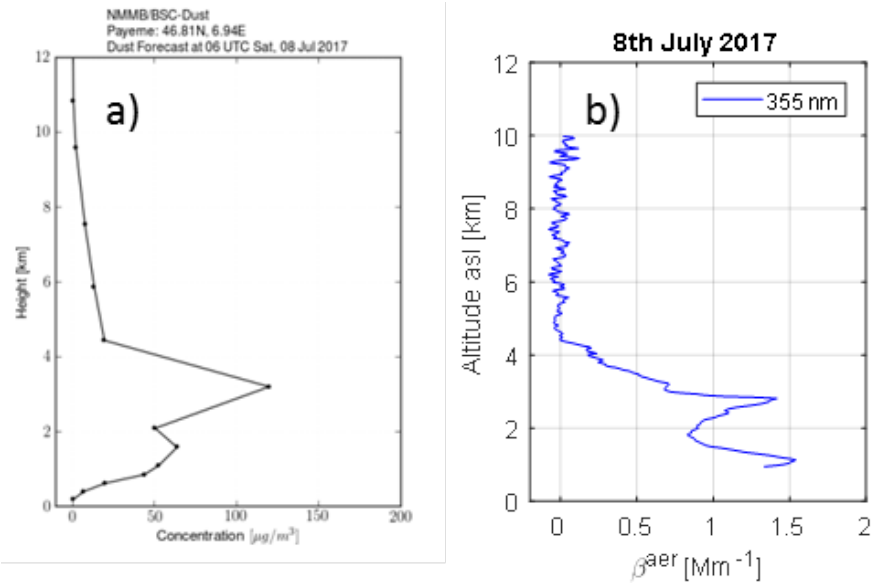

Figure 12. a) Dust concentration profile from NMMB/BSC model forecast at 06 UTC on 8th July 2017 (adapted from http://www.bsc.es/ess/bsc-dust-daily-forecast). b) Vertical profile of β^{aer} at 355 nm from RALMO lidar for the time interval from 01:00 to 01:30 UTC on 8th July 2017.

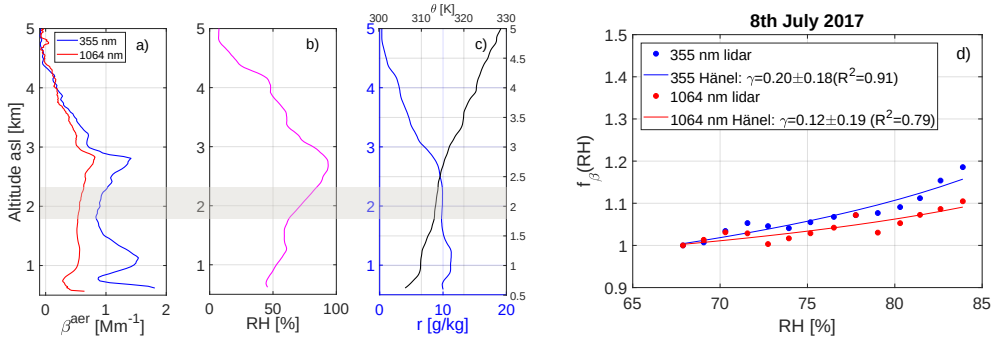

Figure 13. Lidar vertical profiles of (a) β^{aer} at 355 and 1064 nm, (b) *RH* and (c) θ and r obtained between 01:00 and 01:30 on 8th July 2017. (d) f_β at 355 and 1064 nm retrieved for that profiles.

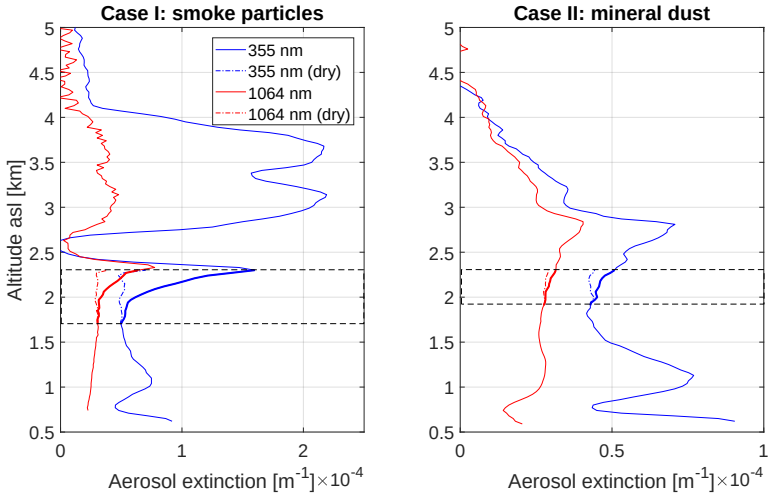

Figure 14. Aerosol extinction profiles at 355 and 1064 nm considering wet (ambient) and dry conditions (in the layer with aerosol hygroscopicity, colored dashed lines) for Case I (left panel) and Case II (right panel). Horizontal dashed black lines indicate the layer for each case in which hygroscopic growth occurred.